


Article

Size and Shape Effects on Fatigue Behavior of G20Mn5QT Steel from Axle Box Bodies in High-Speed Trains

Zhenxian Zhang¹, Zhongwen Li¹, Han Wu^{2,3} and Chengqi Sun^{2,3,*} 

¹ CRRC Qingdao Sifang Co., Ltd., Qingdao 266111, China; zhangzhenxian@cqsf.com (Z.Z.); lzhu1980@163.com (Z.L.)

² State Key Laboratory of Nonlinear Mechanics, Institute of Mechanics, Chinese Academy of Sciences, Beijing 100190, China; wuhan@lnm.imech.ac.cn

³ School of Engineering Science, University of Chinese Academy of Sciences, Beijing 100049, China

* Correspondence: scq@lnm.imech.ac.cn; Tel.: +86-10-8254-3968

Abstract: In this paper, the axial loading fatigue tests are at first conducted on specimens of G20Mn5QT steel from axle box bodies in high-speed trains. Then, the size and shape effects on fatigue behavior are investigated. It is shown that the specimen size and shape have an influence on the fatigue performance of G20Mn5QT steel. The fatigue strength of the hourglass specimen is higher than that of the dogbone specimen due to its relatively smaller highly stressed region. Scanning electron microscope observation of the fracture surface and energy dispersive X-ray spectroscopy indicate that the specimen size and shape have no influence on the fatigue crack initiation mechanism. Fatigue cracks initiate from the surface or subsurface of the specimen, and some fracture surfaces present the characteristic of multi-site crack initiation. Most of the fatigue cracks initiate from the pore defects and alumina inclusions in the casting process, in which the pore defects are the main crack origins. The results also indicate that the probabilistic control volume method could be used for correlating the effects of specimen size and shape on the fatigue performance of G20Mn5QT steel for axle box bodies in high-speed trains.



Citation: Zhang, Z.; Li, Z.; Wu, H.; Sun, C. Size and Shape Effects on Fatigue Behavior of G20Mn5QT Steel from Axle Box Bodies in High-Speed Trains. *Metals* **2022**, *12*, 652. <https://doi.org/10.3390/met12040652>

Academic Editor: Denis Benasciutti

Received: 7 March 2022

Accepted: 9 April 2022

Published: 11 April 2022

Publisher's Note: MDPI stays neutral with regard to jurisdictional claims in published maps and institutional affiliations.



Copyright: © 2022 by the authors. Licensee MDPI, Basel, Switzerland. This article is an open access article distributed under the terms and conditions of the Creative Commons Attribution (CC BY) license (<https://creativecommons.org/licenses/by/4.0/>).

Keywords: G20Mn5QT steel; crack initiation mechanism; fatigue strength; size effect; shape effect

1. Introduction

The high-speed railway industry has developed rapidly in the past decade. Fatigue failure, as one of the main failure modes for engineering materials and components [1–5], is also a key mechanical problem for high-speed trains. Many studies concerning the fatigue problems in high-speed trains have been carried out [6–11]. For example, Lu et al. [12] studied the very-high-cycle fatigue behavior of an axle steel LZ50 under rotating bending fatigue loading and showed that LZ50 steel had the fatigue limit at $5 \times 10^6 \sim 10^9$ cycles. The fatigue fracture surface observation indicated that the fatigue crack initiated from the ferrite on the surface of the specimen. Chen et al. [13] investigated the high cycle and very-high-cycle fatigue performance of an axle steel EA4T, and found that there was still a conventional fatigue limit for EA4T steel. Beretta et al. [14] studied the corrosion fatigue behavior of an axle steel A1N exposed in rainwater, and the results showed that the rainwater significantly reduced the fatigue strength ($>10^6$ cycles) of the A1N steel. Wang et al. [15] analyzed the fatigue strength of the CRH2 motor bogie frame through simulation and online tests. Zhang et al. [16] studied the fatigue crack growth behavior in the gradient microstructure of the surface layer of S38C axle steel. The results indicated that the crack growth rate firstly decelerated and then accelerated with increasing the crack length in the gradient layer. Guagliano and Vergani [17] conducted experiments and numerical analysis on the sub-surface cracks in railway wheels. Gao et al. [18] studied the effect of artificial defects on the fatigue strength of an induction hardened S38C axle and showed that the influence of shallower impact damage (smaller than 200 μm) on fatigue

strength was negligible. Luke et al. [19] made conclusions on some important aspects and results related to the application of the fracture mechanics approach to the prediction of inspection intervals of railway axles under in-service conditions.

The specimen geometry is an important factor affecting fatigue properties [20–22]. The fatigue performance tends to decrease with the increase of specimen size [23,24]. The size and shape of actual components are usually different from the standard testing specimens. Therefore, studying the size and shape effects on the fatigue behavior of materials in key structures of high-speed trains has scientific significance and application value. Li et al. [25] studied the effects of specimen size and notch on the fatigue properties of an EA4T axle steel. The study indicated that, with the increase of specimen size, the fatigue strength of the dogbone specimen was considerably lower than that of the hourglass specimen under axial loading. Shen et al. [26] analyzed the effect of inclusion size on the fatigue strength of small specimens and railway axles, and showed that, due to the increase of risk volume, the critical stress of fatigue failure in axles induced by inclusion was about 50% of that in small specimens under rotating bending loading. Varfolomeev et al. [27] studied the effect of specimen shape on the fatigue crack growth rate of an EA4T axle steel and showed that the crack growth rate depended on the specimen shape and loading condition.

Axle box bodies are important components in high-speed trains, which are subject to cyclic loadings and might fail in service. However, there are few results available for the effects of specimen size and shape on the fatigue behavior of materials for axle box bodies. Therefore, revealing the size and shape effects on the fatigue behavior of materials for axle box bodies is of great importance. This paper studies G20Mn5QT steel from axle box bodies in high-speed trains. The axial loading fatigue tests are at first conducted on the specimens with different size and shape. Then, the fatigue failure mechanism of G20Mn5QT steel is studied based on the observation of the fracture surface by scanning electron microscope (SEM) and the analysis of the crack initiation region by energy dispersive X-ray spectroscopy (EDS). Finally, the size and shape effects on the fatigue performance are correlated by using the probabilistic control volume method for G20Mn5QT steel.

2. Materials and Methods

The material used is a G20Mn5QT steel cut from the new axle box bodies of a high-speed train. The chemical composition is 0.18 C, 0.34 Si, 1.20 Mn, 0.22 Ni, 0.065 Al, 0.03 Cr, 0.011 Cu, 0.017 P, and 0.009 S in weight percent (Fe balance). The axle box body was at first heated at $910 \pm 10^\circ$ for 3.5 h and oil quenched, and then it was tempered for 4 h at $640 \pm 10^\circ$ and cooled to below 300°C with the furnace and then air cooled. The average tensile strength and yield strength of the material are 582 MPa and 399 MPa, respectively. The standard deviation is 0.58 for the tensile strength and 5.5 for the yield strength. They are obtained from three specimens by an MTS Landmark machine. The strain rate is $5 \times 10^{-4} \text{ s}^{-1}$. The shape of the tension specimen is shown in Figure 1a. Fatigue tests were conducted on an MTS Landmark machine. The loading frequency is 1 Hz to 32 Hz and the stress ratio R is -1 . Two kinds of specimens, the hourglass specimen and the dogbone specimen, are chosen for fatigue tests, as shown in Figure 1b,c, respectively. The elastic stress concentration factor K_t is defined as the ratio of the maximum principal stress at the notch root to that of the cylindrical specimen with the same smallest cross section (i.e., nominal stress), and is obtained by using Abaqus 6.14 software. In the calculation, Young's modulus is $E = 210 \text{ GPa}$ and Poisson's ratio is $\nu = 0.3$. All tests were carried out at room temperature in air. Before the fatigue test, the surface of the experimental section of the specimen was ground and polished. The surface roughness R_a was less than $0.5 \mu\text{m}$.

SEM is used to observe the fatigue fracture surface and analyze the crack initiation mechanism. EDS is conducted to determine the element composition in the typical crack initiation region.

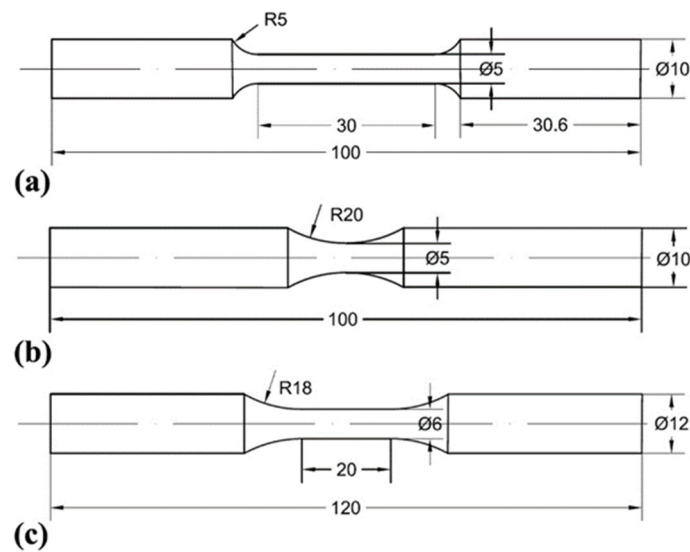


Figure 1. Shape and dimension of specimens (in mm). (a) Tensile specimen; (b) hourglass specimen, $K_t = 1.05$; (c) dogbone specimen.

3. Results

3.1. Measurement of Specimen Temperature

A thermocouple was used to measure the surface temperature of the experimental section of several specimens during the fatigue tests, as shown in Figure 2a. The loading frequency was not increased until the measured temperature was stable after a number of fatigue cycles (e.g., 200, 1000, or 3000 cycles). Figure 2b presents the variation of surface temperature of the experimental section with the loading frequency under the normal stress amplitude of 300 MPa, 350 MPa and 380 MPa for the hourglass specimens. The temperature is the stable temperature at the frequency in the abscissa in Figure 2b. It is observed that, with the increase of the loading frequency, the temperature of the experimental section increases remarkably under the stress amplitude of 350 MPa and 380 MPa, whereas it increases slowly under the stress amplitude of 300 MPa. In order to eliminate the possible influence of the temperature increase on fatigue properties during fatigue tests, an appropriate frequency is adopted under different stress amplitudes according to the results in Figure 2b.

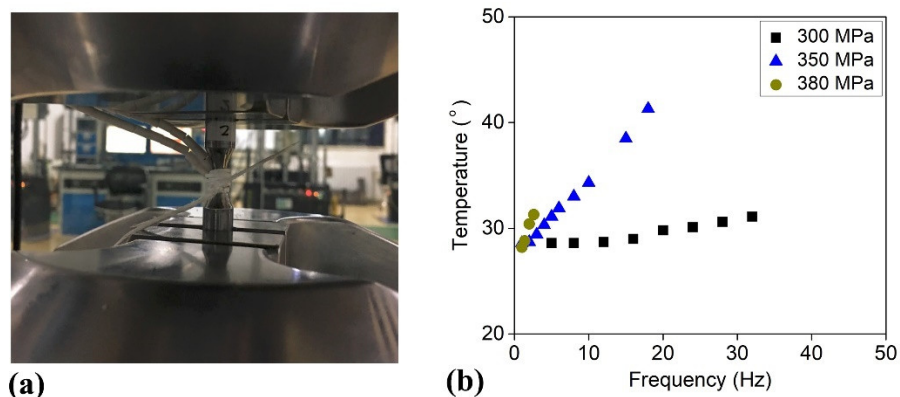


Figure 2. Measurement of surface temperature for experimental section of specimens. (a) Picture of the method for temperature measurement; (b) variation of temperature with loading frequency.

3.2. Stress-Life (S-N) Data

The S-N data of the tested specimens are plotted in Figure 3. Here, the local stress amplitude is used, i.e., the stress concentration is considered for the hourglass specimen.

For the dogbone specimen, the local stress amplitude is the nominal stress amplitude because the positions of the fatigue fracture surface are all at the parallel segment with the smallest section. The loading information of the specimens is listed in Table 1. It is seen from Figure 3 that, with the increase of fatigue life, the fatigue strength decreases for both the hourglass and dogbone specimens. Moreover, the results for a stress amplitude of 367.5 MPa for the hourglass specimen in Figure 3a indicate that the loading frequency has no influence on fatigue performance of the G20Mn5QT steel. Therefore, the effect of loading frequency on the fatigue behavior is not considered for the G20Mn5QT steel when the fatigue data are analyzed in this paper.

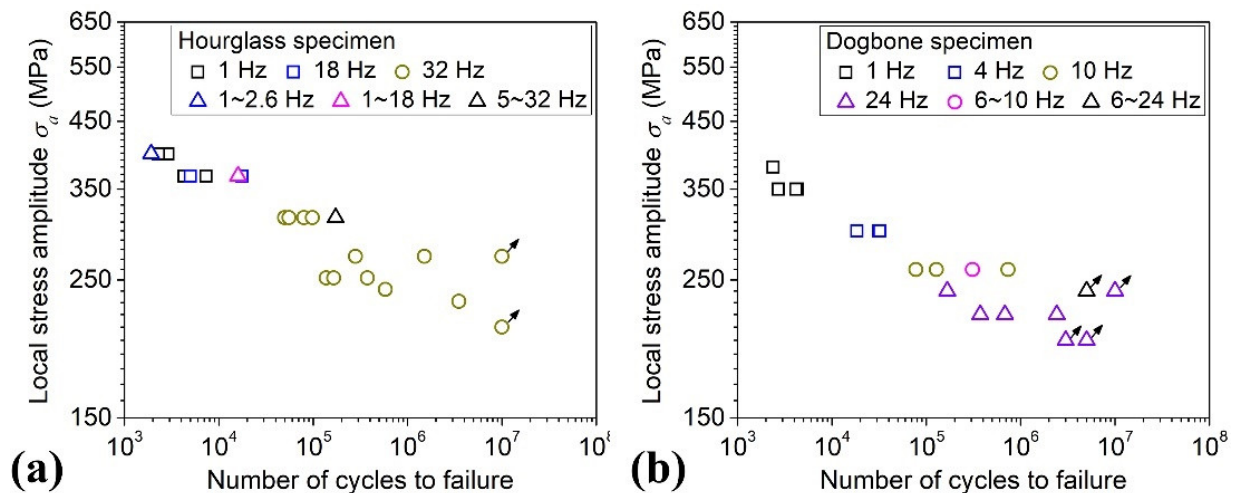


Figure 3. S-N data of the tested specimens, in which the arrows denote the unbroken specimens at the associated cycles. (a) Hourglass specimens; (b) dogbone specimens.

Table 1. Loading information of the tested specimens.

Hourglass Specimens			
No.	Local Stress Amplitude σ_a /MPa	Fatigue Life N /cyc	Loading Frequency f /Hz
1	315	49,889	32
2	367.5	4998	18
3	315	55,521	32
4	367.5	17,677	18
5	399	2895	1
6	399	2299	1
7	273	10,000,000 ¹	32
8	252	374,837	32
9	241.5	581,314	32
10	231	3,495,106	32
11	210	10,000,000 ¹	32
12	252	165,505	32
13	273	280,193	32
14	367.5	7327	1
15	399	1913	1~2.6
16	315	172,615	5~32
17	315	79,551	32
18	315	98,057	32
19	273	1,507,176	32
20	367.5	4271	1
21	367.5	15,993	1~18
22	252	137,278	32

Table 1. Cont.

Dogbone specimens			
No.	Local Stress Amplitude σ_a /MPa	Fatigue Life N /cyc	Loading Frequency f /Hz
1	240	166,822	24
2	300	18,354	4
3	260	127,947	10
4	220	373,935	24
5	350	2704	1
6	350	4156	1
7	260	77,476	10
8	220	2,411,322	24
9	220	691,121	24
10	200	3,000,000 ¹	24
11	200	5,000,000 ¹	24
12	380	2384	1
13	350	4334	1
14	300	31,226	4
15	240	5,000,000 ¹	6~24
16	260	309,419	6~10
17	300	32,059	4
18	260	733,656	10
19	240	10,000,000 ¹	24

¹ Denotes that the specimen does not fail at the associated cycles.

3.3. Crack Initiation Mechanism

Figures 4 and 5 show the SEM images of the fracture surface of several hourglass specimens. It is seen that the fatigue cracks initiate from the specimen surface (Figures 4b and 5b) or the subsurface of the specimen (Figures 4d and 5d). Meanwhile, some specimens exhibit the characteristic of multi-site crack initiation on the fracture surface (Figure 5).

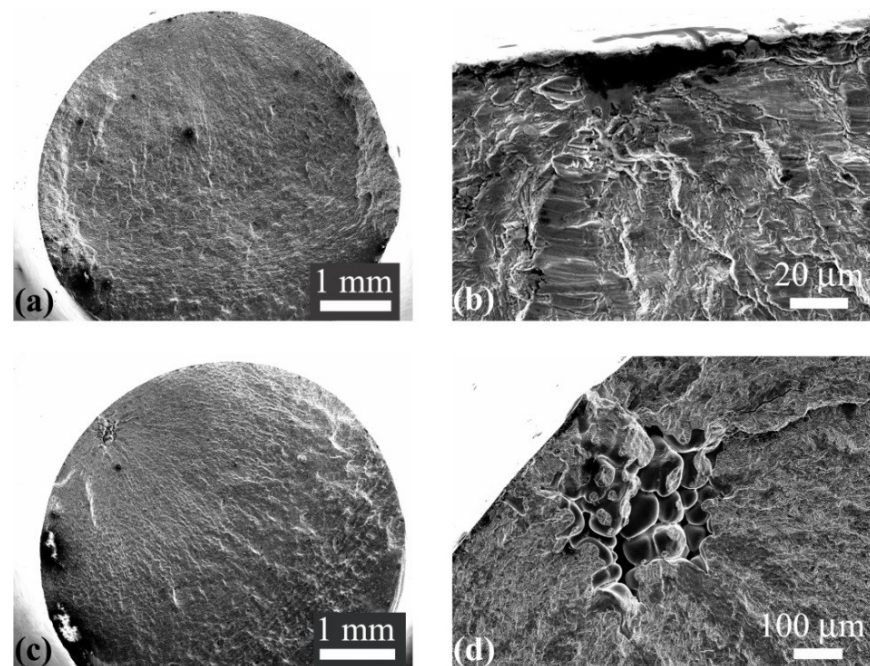


Figure 4. SEM images of the fracture surface for hourglass specimens with single-site crack initiation. (a,b): local stress amplitude $\sigma_a = 315$ MPa, $N = 1.73 \times 10^5$; (c,d): local stress amplitude $\sigma_a = 252$ MPa, $N = 1.37 \times 10^5$.

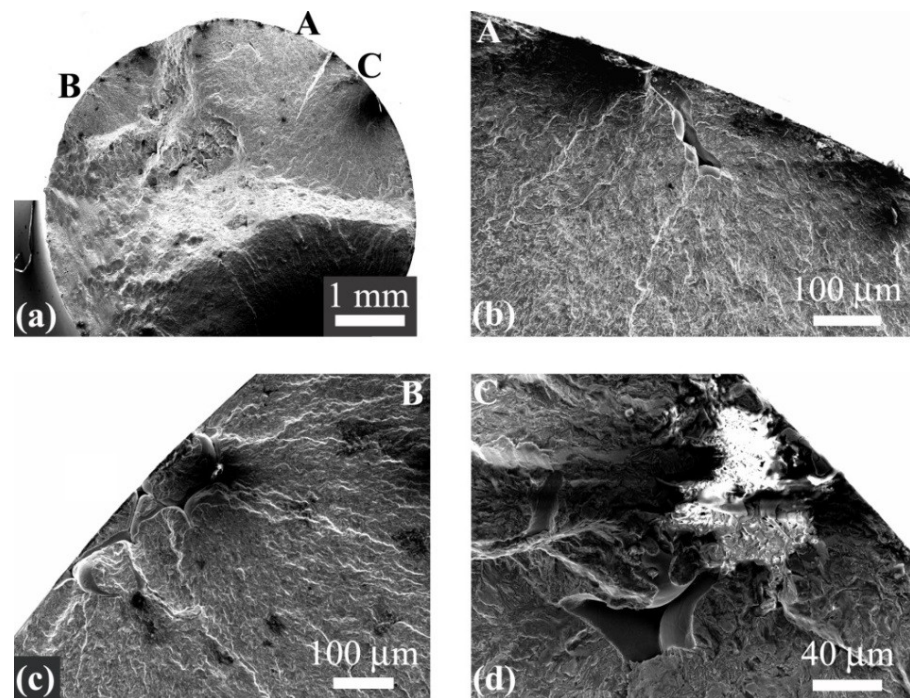


Figure 5. SEM images of the fracture surface for the hourglass specimen with multi-site crack initiation, local stress amplitude $\sigma_a = 315$ MPa, $N = 7.96 \times 10^4$. (a): Fracture surface with low magnification; (b–d): close-ups of crack initiation regions A, B, and C in (a).

SEM images of the fracture surface of several dogbone specimens are shown in Figures 6 and 7. Similar to hourglass specimens, the fatigue cracks initiate from the specimen surface (Figures 6b and 7b) or the subsurface of the specimen (Figure 6d), and some fracture surfaces present the multi-site crack initiation feature (Figure 7).

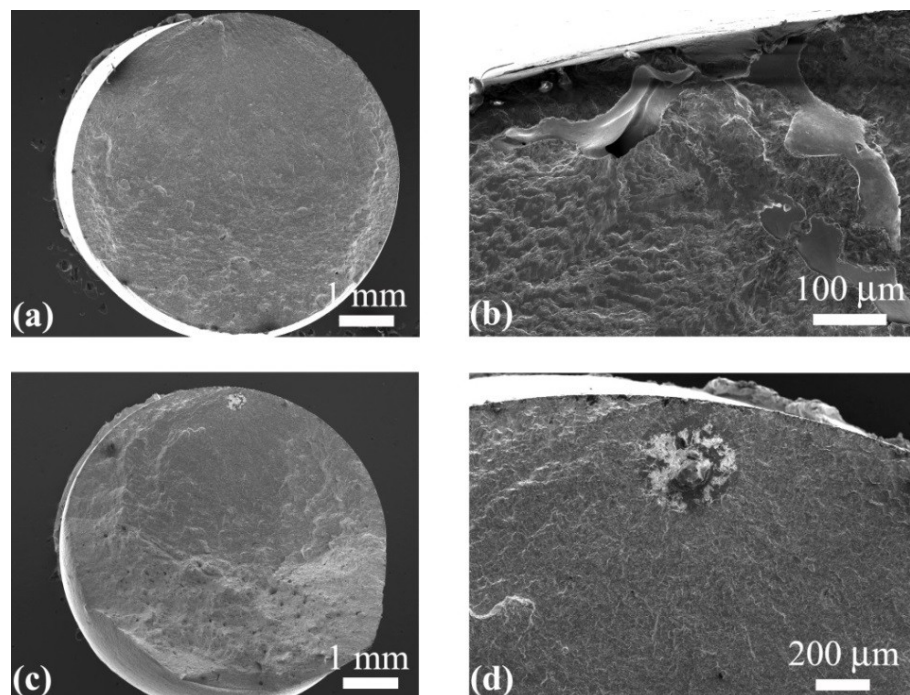


Figure 6. SEM images of the fracture surface for dogbone specimens with single-site crack initiation. (a,b): $\sigma_a = 220$ MPa, $N = 2.41 \times 10^6$; (c,d): $\sigma_a = 350$ MPa, $N = 2.7 \times 10^3$.

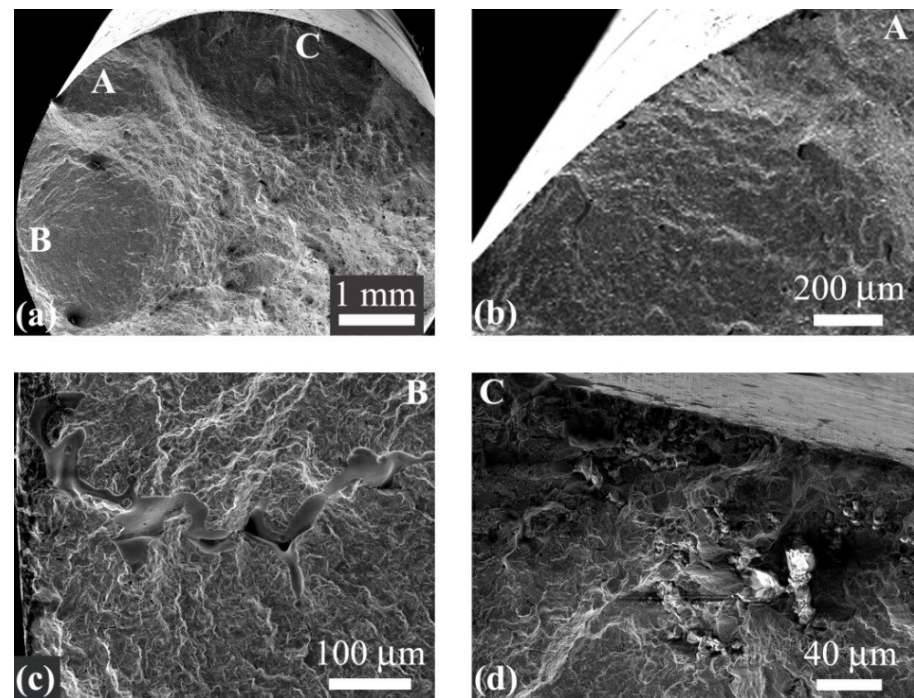


Figure 7. SEM images of the fracture surface for the dogbone specimen with multi-site crack initiation, $\sigma_a = 380$ MPa, $N = 2.38 \times 10^3$. (a): Fracture surface with low magnification; (b–d) Close-ups of crack initiation regions A, B, and C in (a).

The SEM observations show that most fatigue cracks initiate from pore defects (Figures 4d, 5c and 6b) or inclusions (Figures 5d and 6d) for both the hourglass specimen and the dogbone specimen, and pore defects are the main crack initiation origins. The specimen size and shape do not change the fatigue failure mechanism of G20Mn5QT steel. The EDS is further used to determine the composition of the inclusion in the crack initiation region. The accelerating voltage is 15 kV. Figure 8 shows the results for the location “+” in the crack initiation region by EDS. It indicates that the main composition of inclusions should be alumina.

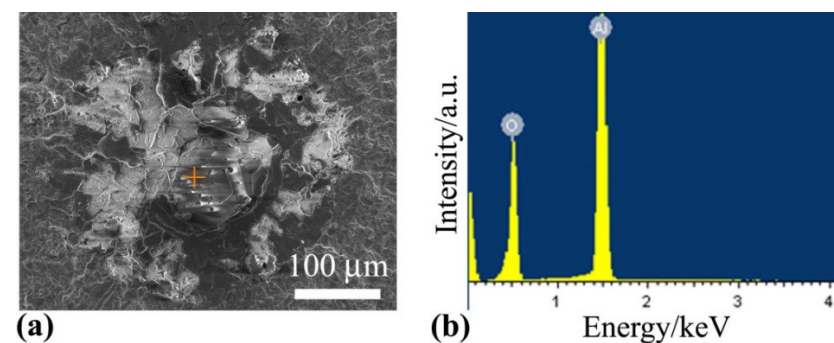


Figure 8. Analysis of composition of the inclusion in crack initiation region in Figure 6d. (a) SEM image of the crack initiation region. The symbol “+” denotes the location analyzed by EDS; (b) result by EDS.

4. Discussion

4.1. Comparison of S-N Data

Figure 9 shows the comparison of the S-N data between hourglass specimens and dogbone specimens. It is seen from Figure 9a that the difference in the S-N data between the two kinds of specimens is not obvious in terms of nominal stress amplitude, while the fatigue life of the hourglass specimen is generally larger than that of the dogbone specimen

for the same local stress amplitude, though the fatigue life data overlap at several low stress amplitudes. As is well-known, the scatter of the fatigue life data tends to be larger at the low stress amplitude (i.e., the long fatigue life). The overlap of the fatigue life data at several low stress amplitudes might be due to the scatter and randomness of the fatigue life. This phenomenon could be explained by the differences among the highly stressed regions of the different types of specimens. The hourglass specimens all fail at or very near the smallest section of the specimen, whereas the positions of the fatigue fracture surface are all located at the parallel segment with the smallest section for the dogbone specimens. The highly stressed region of the hourglass specimen is smaller than that of the dogbone specimen. From the viewpoint of the statistical distribution of microstructures or defects, the dogbone specimen has more possibility for defects or microstructural inhomogeneity that could induce the fatigue failure. This is the reason why the fatigue life of the hourglass specimen is higher than that of the dogbone specimen at the same local stress amplitude. The decrease of the fatigue performance due to the larger highly-stressed region (or control volume) has also been shown for different types of steel in the literature [23,25,26,28–32].

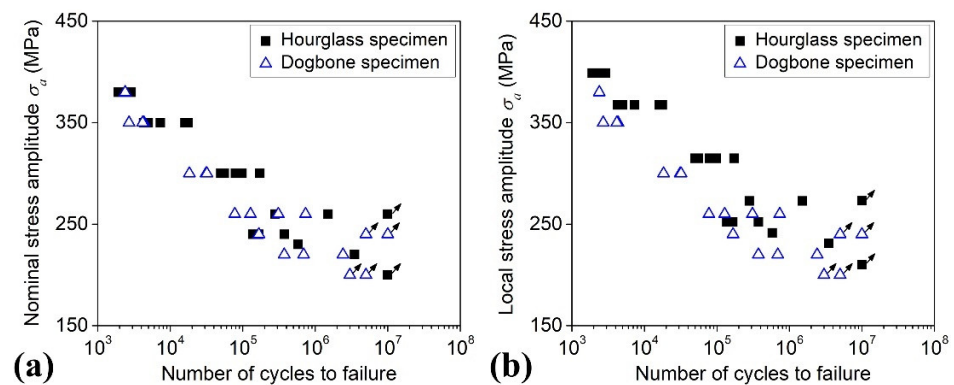


Figure 9. S-N data of specimens with different size and shape, in which the arrows denote the unbroken specimens at the associated cycles. (a) Nominal stress amplitude versus fatigue life; (b) local stress amplitude versus fatigue life.

4.2. Prediction of Size and Shape Effects

Here, the probabilistic control volume method [25,28] is used to analyze the size and shape effects on the fatigue performance of G20MnQT steel. This method considers that if the fatigue strength of specimens A and B can be regarded as the minimum value of many reference specimens with relatively small control volume under the same manufacturing process and heat treatment, and the fatigue strength of the reference specimen follows a Weibull distribution, the fatigue strength of specimens A and B with the same survival probability satisfies the following relation:

$$\frac{\sigma_A - \gamma}{\sigma_B - \gamma} = \left(\frac{V_A}{V_B} \right)^{-\frac{1}{k}} \quad (1)$$

where σ_A and σ_B denote the fatigue strength of specimens A and B, respectively; V_A and V_B denote the control volume, which is usually chosen as the region with no less than 90% of the maximum principal stress [28–32]; $k > 0$ and $\gamma \geq 0$ are shape and location parameters, respectively.

For the case of fatigue failure induced by the surface crack initiation, the following relation is used:

$$\frac{\sigma_A - \gamma}{\sigma_B - \gamma} = \left(\frac{S_A}{S_B} \right)^{-\frac{1}{k}} \quad (2)$$

where S_A and S_B denote the critical part of the specimen surface (i.e., control surface) with a certain thickness.

In particular, for the two-parameter Weibull distribution, the fatigue strength of specimens A and B at the same survival probabilities satisfies the following relation:

$$\frac{\sigma_A}{\sigma_B} = \left(\frac{V_A}{V_B} \right)^{-\frac{1}{k}} \quad (3)$$

$$\frac{\sigma_A}{\sigma_B} = \left(\frac{S_A}{S_B} \right)^{-\frac{1}{k}} \quad (4)$$

From the consideration that the fatigue cracks initiate from the specimen surface or subsurface for all the hourglass and dogbone specimens, Equation (4) is used to analyze the size and shape effects of the fatigue strength for the present G20Mn5QT steel. The control surface (the region where the principal stress is no less than 90% of the maximum principal stress) is obtained by the finite element analysis. In the calculation, the linear elastic constitutive relation is used. The Young's modulus is $E = 210$ GPa and Poisson's ratio is $\nu = 0.3$. At first, the maximum principal stress is calculated at a load of 100 N under the tensile stress, and then the region of the surface of the specimen where the principal stress is no less than 90% of the maximum principal stress is determined. The control surface of the hourglass and dogbone specimens are listed in Table 2. The parameters of the Weibull distribution of the fatigue strength are estimated by the method in the literature [25,28]. In this method, the bilinear model [25,28,33] is assumed for the S-N curve, i.e.,

$$\log_{10} \sigma = \begin{cases} a \log_{10} N + A, & N < N_0 \\ B, & N \geq N_0 \end{cases} \quad (5)$$

where a , A and B are constants, and N_0 is the number of cycles at the knee point of the curve.

Equation (5) can be written as

$$\log_{10} \sigma = \begin{cases} a(\log_{10} N - \log_{10} N_0) + B, & N < N_0 \\ B, & N \geq N_0 \end{cases} \quad (6)$$

For the specimens with the fatigue strength σ_k and the associated fatigue life N_k ($k = 1, 2, \dots, n$, and n is the number of specimens), the values of a , B and N_0 can be obtained by the minimum value of the following equation

$$\sum_{N_k < N_0} [\log_{10} \sigma_k - a \log_{10}(N_k/N_0) - B]^2 + \sum_{N_k \geq N_0} (\log_{10} \sigma_k - B)^2 \quad (7)$$

From Equation (6), the fatigue strength σ_k at an arbitrary fatigue life N_k can be transformed into the fatigue strength σ'_k at a given fatigue life N'_k , i.e.,

$$\log_{10} \sigma'_k = \begin{cases} a \log_{10} \frac{N'_k}{N_k} + \log_{10} \sigma_k, & N_k < N_0 \\ a \log_{10} \frac{N'_k}{N_0} + \log_{10} \sigma_k, & N_k \geq N_0 \end{cases} \quad \text{for } N'_k < N_0 \quad (8)$$

or

$$\log_{10} \sigma'_k = \begin{cases} a \log_{10} \frac{N_0}{N_k} + \log_{10} \sigma_k, & N_k < N_0 \\ \log_{10} \sigma_k, & N_k \geq N_0 \end{cases} \quad \text{for } N'_k \geq N_0 \quad (9)$$

Then, the statistical analysis can be performed for the fatigue strength at different fatigue life and the probabilistic stress-life (P-S-N) curve is obtained.

Figure 10 shows the comparison between the predicted P-S-N curves and the experimental data for the hourglass specimen. It is seen that the predicted 50% survival probability curve is in the middle of the experimental data and almost all the experimental data are within the predicted 5% and 95% survival probability curves. This indicates that the predicted results accord well with the experimental data, namely that the method

in the literature [25,28] is reasonable for the estimation of the parameters of the Weibull distribution of fatigue strength.

Table 2. Control surface of specimens with different size and shape.

Specimen Type	Hourglass	Dogbone
Control surface/mm ²	73.58	498.14

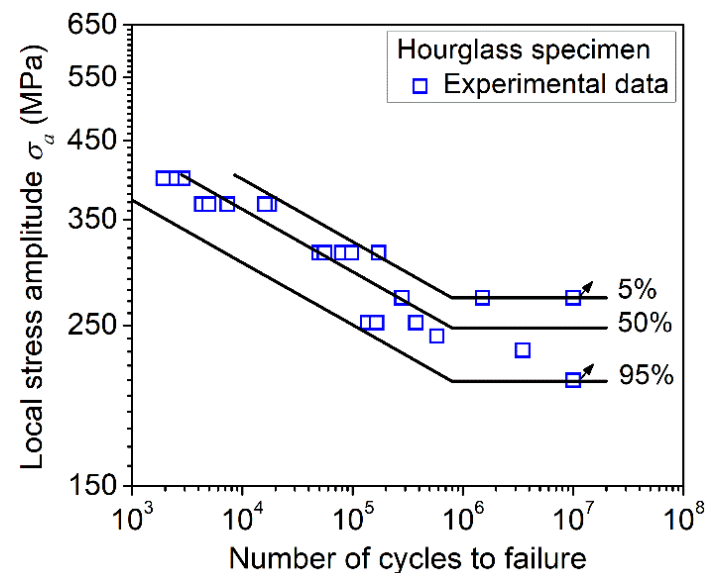


Figure 10. Comparison of predicted P-S-N curves with experimental data for hourglass specimens, in which the arrows denote the unbroken specimens at the associated cycles.

Figure 11 shows the comparison between the predicted P-S-N curves by the experimental data of the hourglass specimen and the experimental data for the dogbone specimen. It is seen that the predicted P-S-N curves are in agreement with the experimental data, indicating that the probabilistic control volume method is applicable for correlating the size and shape effects on the fatigue performance of G20Mn5QT steel.

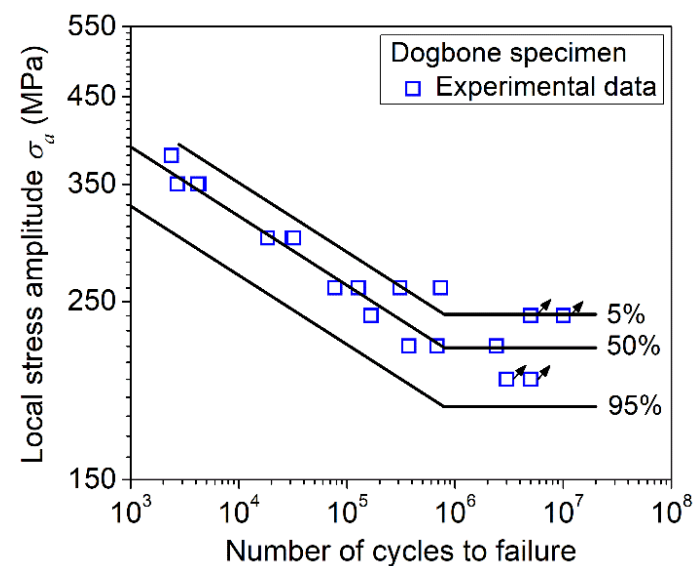


Figure 11. Comparison of predicted P-S-N curves with experimental data of dogbone specimens by using the experimental data of hourglass specimens, in which the arrows denote the unbroken specimens at the associated cycles.

5. Conclusions

In this paper, the size and shape effects on the fatigue behavior are investigated for G20Mn5QT steel of axle box bodies in high-speed trains. The main results are as follows:

The specimen size and shape have influence on the position of the fatigue fracture surface. For the hourglass specimen, it fails at or very near the smallest section of the specimen; whereas for the dogbone specimen, the positions of the fatigue fracture surface are all located at the parallel segment with the smallest section.

The specimen size and shape have no influence on the fatigue failure mechanism of G20Mn5QT steel under an axial loading fatigue test. The fatigue cracks initiate from the surface or the subsurface of the specimen, and some fatigue fracture surfaces exhibit the characteristic of multi-site crack initiation. Most of the fatigue cracks initiate from the pore defects and alumina inclusions in the casting process, and the pore defects are the main crack origins.

The specimen size and shape have an influence on the fatigue performance of G20Mn5QT steel. Due to the larger highly stressed region, the fatigue life of the hourglass specimen is generally higher than that of the dogbone specimen at the same local stress amplitude. The probabilistic control volume method is applicable to correlating the size and shape effects on the fatigue performance of G20Mn5QT steel.

The results are helpful in understanding the fatigue failure mechanism of G20Mn5QT steel and the size and shape effects on the fatigue behavior of metallic materials.

Author Contributions: Conceptualization, Z.Z., Z.L. and C.S.; investigation, Z.Z., Z.L. and C.S.; visualization, Z.L., H.W. and C.S.; writing—original draft preparation, Z.Z., Z.L., H.W. and C.S.; writing—review and editing, Z.Z., Z.L., H.W. and C.S.; supervision, C.S. All authors have read and agreed to the published version of the manuscript.

Funding: This research was funded by the National Key Research and Development Program of China (2017YFB0304600).

Institutional Review Board Statement: Not applicable.

Informed Consent Statement: Not applicable.

Data Availability Statement: Data sharing is not applicable.

Conflicts of Interest: The authors declare no conflict of interest.

References

1. Li, G.; Sun, C.Q. High-temperature failure mechanism and defect sensitivity of TC17 titanium alloy in high cycle fatigue. *J. Mater. Sci. Technol.* **2022**, *122*, 128–140. [[CrossRef](#)]
2. Rozumek, D.; Faszynka, S. Surface cracks growth in aluminum alloy AW-2017A-T4 under combined loadings. *Eng. Fract. Mech.* **2020**, *226*, 106896. [[CrossRef](#)]
3. Sun, C.Q.; Li, Y.Q.; Xu, K.L.; Xu, B.T. Effects of intermittent loading time and stress ratio on dwell fatigue behavior of titanium alloy Ti-6Al-4V ELI used in deep-sea submersibles. *J. Mater. Sci. Technol.* **2021**, *77*, 223–236. [[CrossRef](#)]
4. Rozumek, D. Influence of the slot inclination angle in FeP04 steel on fatigue crack growth under tension. *Mater. Des.* **2009**, *30*, 1859–1865. [[CrossRef](#)]
5. Lukács, J.; Meilinger, Á.; Pósalaky, D. High cycle fatigue and fatigue crack propagation design curves for 5754-H22 and 6082-T6 aluminium alloys and their friction stir welded joints. *Weld. World* **2018**, *62*, 737–749. [[CrossRef](#)]
6. Mädler, K.; Geburtig, T.; Ullrich, D. An experimental approach to determining the residual lifetimes of wheelset axles on a full-scale wheel-rail roller test rig. *Int. J. Fatigue* **2016**, *86*, 58–63. [[CrossRef](#)]
7. Wang, Y.; Yuan, L.; Zhang, S.; Sun, C.; Wang, W.; Yang, G.; Wei, Y. The influence of combined gradient structure with residual stress on crack-growth behavior in medium carbon steel. *Eng. Fract. Mech.* **2019**, *209*, 369–381. [[CrossRef](#)]
8. Wu, S.C.; Liu, Y.X.; Li, C.H.; Kang, G.Z.; Liang, S.L. On the fatigue performance and residual life of intercity railway axles with inside axle boxes. *Eng. Fract. Mech.* **2018**, *197*, 176–191. [[CrossRef](#)]
9. Akama, M. Bayesian analysis for the results of fatigue test using full-scale models to obtain the accurate failure probabilities of the Shinkansen vehicle axle. *Reliab. Eng. Syst. Safe* **2002**, *75*, 321–332. [[CrossRef](#)]
10. Xu, Y.H.; Zhao, Y.X. Simulation for short fatigue cracks initiation of LZ50 axle steel for railway vehicles. *Chin. J. Appl. Mech.* **2009**, *26*, 589–593.

11. Cervello, S. Fatigue properties of railway axles: New results of full-scale specimens from Euraxles project. *Int. J. Fatigue* **2016**, *86*, 2–12. [[CrossRef](#)]
12. Lu, L.T.; Zhang, J.W.; Zhang, Y.B.; Zhi, B.Y.; Zhang, W.H. Rotary bending fatigue property of LZ50 axle steel in gigacycle regime. *J. China Railw. Soc.* **2009**, *31*, 37–41.
13. Chen, Y.P.; Li, Y.B.; Zhang, X.L.; Sun, C.Q.; Hong, Y.S. Study on high-cycle and very-high-cycle fatigue properties of EA4T axle steel. *Rail Transp. Equip. Technol.* **2017**, *1*, 21–23.
14. Beretta, S.; Carboni, M.; Fiore, G.; Lo Conte, A. Corrosion–fatigue of A1N railway axle steel exposed to rainwater. *Int. J. Fatigue* **2010**, *32*, 952–961. [[CrossRef](#)]
15. Wang, W.J.; Liu, Z.M.; Li, Q.; Miao, L.X. Fatigue strength analysis of CRH2 motor bogie frame. *J. Beijing Jiaotong Univ.* **2009**, *33*, 5–9.
16. Zhang, S.J.; Xie, J.J.; Jiang, Q.Q.; Zhang, X.L.; Sun, C.Q.; Hong, Y.S. Fatigue crack growth behavior in gradient microstructure of hardened surface layer for an axle steel. *Mater. Sci. Eng. A* **2017**, *700*, 66–74. [[CrossRef](#)]
17. Guagliano, M.; Vergani, L. Experimental and numerical analysis of sub-surface cracks in railway wheels. *Eng. Fract. Mech.* **2005**, *72*, 255–269. [[CrossRef](#)]
18. Gao, J.W.; Pan, X.N.; Han, J.; Zhu, S.P.; Liao, D.; Li, Y.B.; Dai, G.Z. Influence of artificial defects on fatigue strength of induction hardened S38C axles. *Int. J. Fatigue* **2020**, *139*, 105746. [[CrossRef](#)]
19. Luke, M.; Varfolomeev, I.; Lütkepohl, K.; Esderts, A. Fatigue crack growth in railway axles: Assessment concept and validation tests. *Eng. Fract. Mech.* **2011**, *78*, 714–730. [[CrossRef](#)]
20. Tomaszewski, T.; Sempruch, J. Analysis of size effect in high-cycle fatigue for EN AW-6063. *Solid State Phenom.* **2014**, *224*, 75–80. [[CrossRef](#)]
21. Lee, Y.L.; Pan, J.; Hathaway, R.; Barkey, M. *Fatigue Testing and Analysis: Theory and Practice*; Elsevier Butterworth-Heinemann: Oxford, UK, 2005.
22. Li, Y.Q.; Song, Q.Y.; Feng, S.C.; Sun, C.Q. Effects of loading frequency and specimen geometry on high cycle and very high cycle fatigue life of a high strength titanium alloy. *Materials* **2018**, *11*, 1628. [[CrossRef](#)] [[PubMed](#)]
23. Furuya, Y. Specimen size effects on gigacycle fatigue properties of high-strength steel under ultrasonic fatigue testing. *Scr. Mater.* **2008**, *58*, 1014–1017. [[CrossRef](#)]
24. Shirani, M.; Härkegård, G. Fatigue life distribution and size effect in ductile cast iron for wind turbine components. *Eng. Fail. Anal.* **2011**, *18*, 12–24. [[CrossRef](#)]
25. Li, Y.B.; Song, Q.Y.; Yang, K.; Chen, Y.P.; Sun, C.Q.; Hong, Y.S. Probabilistic control volume method for the size effect of specimen fatigue performance. *Chin. J. Theor. App. Mech.* **2019**, *51*, 1363–1371. [[CrossRef](#)]
26. Shen, X.L.; Lu, L.T.; Jiang, H.F.; Zhang, J.W.; Yi, H.F. Effect of inclusion size on the fatigue strength of small specimens and railway alloy axles. *J. Mech. Eng.* **2010**, *46*, 48–52. [[CrossRef](#)]
27. Varfolomeev, I.; Luke, M.; Burdack, M. Effect of specimen geometry on fatigue crack growth rates for the railway axle material EA4T. *Eng. Fract. Mech.* **2011**, *78*, 742–753. [[CrossRef](#)]
28. Sun, C.Q.; Song, Q.Y. A method for predicting the effects of specimen geometry and loading condition on fatigue strength. *Metals* **2018**, *8*, 811. [[CrossRef](#)]
29. Murakami, Y. *Metal Fatigue: Effects of Small Defects and Nonmetallic Inclusions*; Elsevier Science Ltd.: Oxford, UK, 2002; pp. 333–336.
30. Sun, C.Q.; Zhang, X.; Liu, X.; Hong, Y.S. Effects of specimen size on fatigue life of metallic materials in high-cycle and very-high-cycle fatigue regimes. *Fatigue Fract. Eng. Mater. Struct.* **2016**, *39*, 770–779. [[CrossRef](#)]
31. Sun, C.Q.; Song, Q.Y. A method for evaluating the effects of specimen geometry and loading condition on fatigue life of metallic materials. *Mater. Res. Express* **2019**, *6*, 046536. [[CrossRef](#)]
32. Li, C.M.; Hu, Z.; Sun, C.Q.; Song, Q.Y.; Zhang, W.H. Probabilistic control volume method for evaluating the effects of notch size and loading type on fatigue life. *Acta Mech. Solida Sin.* **2020**, *33*, 141–149. [[CrossRef](#)]
33. Hanaki, S.; Yamashita, M.; Uchida, H.; Zako, M. On stochastic evaluation of S–N data based on fatigue strength distribution. *Int. J. Fatigue* **2010**, *32*, 605–609. [[CrossRef](#)]